Atmos. Meas. Tech. Discuss., https://doi.org/10.5194/amt-2017-438
Manuscript under review for journal Atmos. Meas. Tech.
Discussion started: 15 December 2017


Atmospheric Measurement Techniques Discussions

# New method to determine the instrument spectral response function, applied to TROPOMI-SWIR

Richard M. van Hees[1], Paul J. J. Tol[1], Sidney Cadot[1,2], Matthijs Krijger[1,3], Stefan T. Persijn[5], Tim A. van Kempen[1], Ralph Snel[1,4], Ilse Aben[1], and Ruud W. M. Hoogeveen[1]

[1]SRON Netherlands Institute for Space Research, Utrecht, the Netherlands
[2]Jigsaw B.V., Delft, the Netherlands
[3]Earth Space Solutions, Utrecht, the Netherlands
[4]Science and Technology B.V., Delft, the Netherlands
[5]VSL Dutch Metrology Institute, Delft, the Netherlands

*Correspondence to:* Dr Richard van Hees (r.m.van.hees@sron.nl)

**Abstract.** The Tropospheric Monitoring Instrument (TROPOMI) is the single instrument on board of the ESA Copernicus Sentinel-5 Precursor satellite. TROPOMI is a nadir-viewing imaging spectrometer with bands in the ultraviolet and visible, the near infrared and the short-wave infrared (SWIR). An accurate instrument spectral response function (ISRF) is required in the SWIR band where absorption lines of CO, methane and water vapor overlap. Therefore a novel method for ISRF determination for an imaging spectrometer was developed and applied to the TROPOMI-SWIR band. The ISRF of all detector pixels of the SWIR spectrometer has been measured during an on-ground calibration campaign. The accuracy of the derived ISRF is well within the requirement for accurate trace-gas retrievals. Long-term in-flight monitoring of the ISRF is guaranteed by the presence of five SWIR diode lasers.

## 1 Introduction

The Tropospheric Monitoring Instrument (TROPOMI) is the single payload of the Copernicus Sentinel-5 Precursor (S5P) satellite mission (Veefkind et al., 2012). The instrument maps the Earth's atmosphere in two dimensions using two spectrometer modules, one covering the ultraviolet / visible (270–495 nm) and near-infrared (675–775 nm), and the other covering the short-wave infrared (SWIR) spectral range 2305–2385 nm. The latter with a spectral resolution of 0.25 nm and a spectral sampling distance of 0.1 nm. The SWIR spectrometer (developed by SSTL, United Kingdom) consists of a slit, collimator mirror optics, an immersed grating (developed by SRON, van Amerongen et al. (2012)), anamorphic prism and camera optics consisting of multiple lenses, and a HgCdTe detector (developed by Sofradir, France). The detector has 1000 columns in the spectral dimension and 256 rows in the spatial dimension of which about 216 rows and 984 columns are nominally illuminated.

The TROPOMI-SWIR band is used for the retrieval of atmospheric CO and methane columns. The methane concentrations have to be measured with an accuracy of better than 1%. Therefore, the requirement on systematic errors is very strict. Simulations have shown that the methane retrieval is very sensitive to errors in the instrument spectral response function (ISRF), which is used to include the measured absorption line shape in the modeled Earth spectra (Hu et al., 2016). Therefore, the

Atmos. Meas. Tech. Discuss., https://doi.org/10.5194/amt-2017-438
Manuscript under review for journal Atmos. Meas. Tech.
Discussion started: 15 December 2017


Atmospheric Measurement Techniques Discussions

requirement on the ISRF is that it should be known with an accuracy of 1% of its maximum where the ISRF is greater than 1% of its maximum (Buscaglione, 2011; Hu et al., 2016). To reach the required accuracy, the ISRF has been measured with high spectral resolution during on-ground calibration measurements using a scanning monochromatic light source covering the SWIR band.

In the literature, the instrument spectral *spread* function (ISSF) and instrument spectral *response* function (ISRF) are often confused. In this paper, we define a "spread function" and a "response function" as follows: a "spread function" maps an object to image space, which involves many detector pixels; a "response function" maps an image to object space, which is a property of a given detector pixel. The ISSF is measured simply by illuminating the spectrometer slit homogeneously with a monochromatic source and taking a detector image (frame). In the spectral dimension, about 4–5 points have significant signal. This is the spread function of the instrument for this wavelength. In Fig. 1b it is shown as a red cross section. When the wavelength is scanned in small steps over a set of frames, the signal in those frames for a given pixel (that is illuminated in at least some of the frames) forms an ISRF, with an arbitrarily fine sampling. This is shown as a green cross section in Fig. 1c. There is an infinite number of ISSFs (one at each wavelength) and a finite number of ISRFs (one for each pixel).

The ISSF consists of one sample from each ISRF of a few neighboring pixels on a row. If the ISRF varies negligibly between these pixels, the ISSF is a sparsely sampled version of this ISRF. However, Fig. 1a shows that the samples taken with increasing column index are ISRF points from the right side of the peak to the left side: the ISSF samples a mirrored ISRF, indicated by the light-green line at bottom left.

During the on-ground calibration measurements, the absolute wavelength of the source is not measured accurately enough. Instead, each frame is seen as the measurement of an ISSF per row, and the column index of the fitted center is used as a wavelength label for the row data. The ISRF of a pixel, based on data from a set of frames, is then the normalized signal as a function of wavelength in pixel units (non-integer values). It should not be confused with the ISSF, which has basically the same horizontal scale but then in integer pixel values. Only at the end of the algorithm is the ISRF of a given pixel converted to a function of wavelength in nm, using the wavelength assignment derived from an independent wavelength calibration measurement. This results in the ISRF calibration key data (CKD) which are used in trace-gas retrievals.

The measurements used for the ISRF characterization are presented in Sect. 2. A description of the method and algorithm used to derive the ISRF for all illuminated pixels is presented in Sect. 3. Details of the algorithm are discussed in Sect. 4, where we also present the ISRF analysis based on the on-ground calibration measurements. The validation of the irradiance ISRF using the radiance measurements is discussed at the end of Sect. 4. The in-flight monitoring of the ISRF is briefly described in Sect. 5.

## 2 Calibration measurements

In this section, we describe the setup used during the ISRF calibration measurements, performed at the Centre Spatial de Liège (CSL) in Belgium, during the on-ground calibration campaign (Kleipool et al., 2017). In this setup, the light source employed is a 2 W continuous-wave optical parametric oscillator (OPO), custom-built by VSL (Delft, the Netherlands). The OPO is pumped

Atmos. Meas. Tech. Discuss., https://doi.org/10.5194/amt-2017-438
Manuscript under review for journal Atmos. Meas. Tech.
Discussion started: 15 December 2017


Atmospheric Measurement Techniques Discussions

by a single-frequency distributed feedback fiber laser operating at 1064 nm which is amplified to 10 W by an ytterbium fiber amplifier. The OPO wavelength is set coarsely between 2290 nm and 2390 nm by manually setting the temperature of the periodically poled lithium niobate crystal and rotating the etalon mounted on a galvo. The wavelength is scanned continuously over a range of about 2 nm by applying a changing piezo voltage to the fiber laser and simultaneously changing the crystal temperature with a predetermined dependence on the piezo voltage. To avoid speckle patterns on the detector, the light is sent to an integrating sphere via a high-speed spinning mirror with a small angle between the rotation axis and the normal. The light exits the integrating sphere and is collimated with a field stop and an off-axis parabolic mirror. The instrument is mounted on a cradle in order to scan all swath angles in a range of $108^\circ$ around nadir. The beam corresponds to a swath-angle coverage of $1.1^\circ$, when the radiance port of TROPOMI is used. During irradiance ISRF measurements, the whole swath is illuminated at once via the on-board solar diffuser. With a neutral density filter just after the OPO, the power entering the instrument has been reduced to avoid saturation. During a wavelength scan, the data is collected at 10 Hz during approximately 165 seconds, taking approximately 80 samples. Background measurements are taken by closing a shutter between the filter and the spinning mirror. For more details on the setup, see Tol et al. (2017, Sect. 2).

Calibration measurements via the radiance port and irradiance port have been performed to verify that they are identical. The measurements of the radiance ISRF lasted significantly longer as not only the laser wavelength had to be scanned, but also the swath angle. Therefore, during the radiance ISRF measurements about 100 wavelength scans per manual wavelength setting are performed to cover all swath angles, and due to time constraints one-way wavelength scans were taken. During the irradiance ISRF measurements each wavelength scan was performed up and down.

## 3 Methodology

In this section, we describe our method to characterize the TROPOMI-SWIR ISRF in general. Specific measurement issues will be discussed in Sect. 4.

### 3.1 ISRF shape

To derive the ISRF from the measured ISSF, an assumption has to be made on the shape of the ISRF. In an iterative way, the ISRF shape can be made more complex to fit its detailed features. At the start of the procedure it is assumed that the ISRF is just a convolution of a block distribution with a normal distribution. This corresponds to an image of the slit on the detector (the block), with the optics blurring the image (the normal distribution). In later iterations, the normal distribution is allowed to be skewed. As the measurements show longer spectral tails, a dedicated tail function is added to the ISRF to account for this. For the tails, several functions were tried. In the end, the Pearson type VII distribution resulted in the best fit.

Atmos. Meas. Tech. Discuss., https://doi.org/10.5194/amt-2017-438
Manuscript under review for journal Atmos. Meas. Tech.
Discussion started: 15 December 2017


Atmospheric Measurement Techniques Discussions

Mathematically, the ISRF is modeled by the weighted sum of functions for the peak and the tails. Peak function $\mathcal{S}$ is a skew-normal distribution convolved with a block distribution and tail function $\mathcal{P}_7$ is a Pearson type VII distribution.

$$\begin{aligned}\mathcal{R}(c;d,s,w,\eta,\gamma,m,c_0) =&(1-\eta)\,\mathcal{S}(c;d,s,w,c_0)\\ &+\eta\,\mathcal{P}_7(c;\gamma,m,c_0)\end{aligned} \tag{1}$$

The two constituent distributions have been normalized to area 1, so that weight $\eta$ is the fraction of the total area in the tail function. The weight has to be in the range $0 \le \eta \le 1$. The ISRF model is a function of column index $c$ with its mean at $c_0$, where both are non-integer numbers. The wavelength assignment is performed when the ISRF calibration key data (CKD) are generated: the SWIR wavelength calibration key data are used to assign a wavelength to the center of a pixel and the ISRF is defined relative to that wavelength.

Peak function $\mathcal{S}$ has three shape parameters, the skew-normal width $d$, skewness parameter $s$ and block width $w$:

$$\begin{aligned}\mathcal{S}(c;d,s,w,c_0) =&\frac{\operatorname{erf}\left(\xi_+/\sqrt{2}\right)-\operatorname{erf}\left(\xi_-/\sqrt{2}\right)}{2w}\\ &-2\frac{T(\xi_+,s)-T(\xi_-,s)}{w}\end{aligned} \tag{2}$$

with

$$\xi_\pm = \frac{\sqrt{1-\delta^2}}{d}(c-c_0\pm\tfrac{w}{2})+\delta \quad \text{where} \quad \delta = \frac{\sqrt{2}\,s}{\sqrt{\pi(1+s^2)}}$$

and using Owen's T function (Patefield and Tandy, 2000)

$$T(z,s) = \frac{1}{2\pi}\int_0^s \frac{\exp\left(-\frac{1}{2}z^2(1+t^2)\right)}{1+t^2}\,\mathrm{d}t. \tag{3}$$

Tail function $\mathcal{P}_7$ has two shape parameters, $\gamma$ and $m$:

$$\mathcal{P}_7(c;\gamma,m,c_0) = \frac{\Gamma(m)}{\gamma\sqrt{\pi}\Gamma(m-\frac{1}{2})}\left(1+\frac{(c-c_0)^2}{\gamma^2}\right)^{-m} \tag{4}$$

with $m > 1/2$ and $\gamma > 0$. The specific case $\mathcal{P}_7(c;\gamma,1,c_0)$ is the Lorentz distribution with half width at half-maximum $\gamma$.

### 3.2 Data preparation

The measurement data are corrected for background, pixel response non-uniformity and stray light (irradiance only). Absolute (ir)radiance calibration is not required. Readouts from bad pixels are discarded in the analysis.

The measurement data of each wavelength scan are processed separately. Frames where the light source was off or very weak are discarded. In each remaining frame, the column with the maximum average signal is determined and the columns up to 7 pixels from this peak column are selected, to include the faint signal of the tails.

Atmos. Meas. Tech. Discuss., https://doi.org/10.5194/amt-2017-438
Manuscript under review for journal Atmos. Meas. Tech.
Discussion started: 15 December 2017


Atmospheric Measurement Techniques Discussions

### 3.3 ISSF fit

The ISRF parameters cannot be retrieved directly from the measurements, because the wavelength and intensity of the signal are unknown and have to be determined via the ISSF. The ISSF is assumed to be the mirrored version of an ISRF, which can be modeled with the function $A\mathcal{R}(c; d, -s, w, \eta, \gamma, m, c_0)$ using Eq. (1); only its skew parameter $s$ has the opposite sign. In each frame, the ISSF of an illuminated row is fitted to the ISRF shape to normalize the signals and to find the wavelength peak position expressed in pixel units (Fig. 1b). The normalized signal and the distance to the fitted peak position yields one point of the ISRF shape, illustrated by the intersection of the red and green line in Fig. 1a. The normalized signal as a function of the fitted peak position forms a set of points covering the ISRF shape (Fig. 1c).

### 3.4 ISRF fit

For a specific pixel in a row, each frame yields one ISSF fit and thus one point of the ISRF shape. While scanning the laser and recording frames, the set of points covering the ISRF shape of a given pixel is generated from the ISSF fits. As the laser-wavelength scan is not regular, the ISRF data points are not on a regular grid. Therefore, the points in the scan range are collected in bins of $1/32$ of a spectral pixel and a median is applied to the data points in each bin. Empty bins are discarded. Reducing the number of points like this also speeds up the fitting and reduces noise while no significant details are lost. The ISRF is fitted with the function $A\mathcal{R}(c; d, s, w, \eta, \gamma, m, c_0)$ using Eq. (1).

The quality of the fit is determined by calculating the fit variance, the sum of the squared fit residuals where the fit function is larger than 6% of the maximum, divided by the number of degrees of freedom (number of points minus the free fit parameters). The square root of the fit variance is the rms value.

### 3.5 ISRF parameter smoothing

The ISRF calibration key data has to be valid for the whole SWIR spectral range and for all swath angles. However, the ISRF fits are valid locally (at location $(r, c)$) and not available for all pixels. It is expected that the fit parameters that define the local ISRF vary only smoothly over the surface of the detector as this is determined by the spectrometer optics. Therefore, a bivariate polynomial fitting is used to smooth and to interpolate the ISRF fit parameters. The model with variables $r$ and $c$, where the first row and column are mapped to $-1$ and the last row and column mapped to $+1$, is given by

$$E_{\text{fit}}[r, c; \boldsymbol{a}] = \sum_{k=0}^{M(M+3)/2} a_k T_{m-n}\left(2\frac{r}{255} - 1\right) T_n\left(2\frac{c}{999} - 1\right), \tag{5}$$

using Chebyshev polynomials of the first kind $T_n(x)$ and indices

$$m = \left\lfloor \tfrac{1}{2}\left(\sqrt{1+8k} - 1\right)\right\rfloor,$$
$$n = k - m(m+1)/2.$$

Atmos. Meas. Tech. Discuss., https://doi.org/10.5194/amt-2017-438
Manuscript under review for journal Atmos. Meas. Tech.
Discussion started: 15 December 2017


Atmospheric Measurement Techniques Discussions

To obtain good results for the ISRF parameter fitting, obvious outliers in the individual ISRF-fit results should be rejected before the bivariate polynomial fit is performed. Given the distribution of outliers (in columns at the same wavelength), it is judged that most of them are caused by laser artifacts. The following data selection was applied before the parameter fitting:

- no ISRF fit is performed on the first and last two pixels of an automated scan, because the whole peak of the ISRF should be present in the data;
- curve fit solutions were rejected in case the curve-fitting routine signaled an error. This happened for a small fraction of the pixels ($< 1\,\%$), due to bad ISRF data;
- unrealistic curve-fit solutions are rejected: skew-normal width $d < 0.1$ or skew $|s| > 5$;
- poor fits are rejected based on their rms value. Irradiance measurements: reject data of the whole column when its median rms is larger than 0.0065. Radiance measurements: reject ISRF fits with an rms larger than 0.0065.

The ISRF of a given pixel can sometimes be derived multiple times, because ($i$) the automated scans overlap in wavelength; ($ii$) for irradiance measurements, all automated scans are performed twice: scanning up and down in wavelength. ($iii$) for radiance measurements, successive scans overlap in the swath direction by half a pixel. For the parameter fits, only the ISRF fit with the smallest rms is used.

Orders $M$ of the bivariate Chebyshev expansions applied to the irradiance and radiance data are equal, except in cases of $d$ and $s$. The irradiance data has a better coverage in both spectral and spatial directions, so a higher order $M = 7$ could be applied on the parameters $d$ and $s$, which show much more structure than the other fit parameters. An order $M = 6$ was used on the radiance data. Order M used for $w$, $\gamma$ and $\eta$ are 5, 2 and 2, respectively. The result of this step yields the ISRF parameter models that are employed to calculate the ISRF calibration key data for each and every pixel. These key data are used in the SWIR retrieval algorithms that derive the gas columns.

The quality of the parameter fitting is determined by comparing the measured ISRF data points with the ISRF that results from the parameter model. An $\text{rms}_{\text{model}}$ value is determined in a similar way as the rms defined in Sect. 3.4. In general, the parameter smoothing will result in better and smoother ISRF calibration key data due to averaging and interpolation. Possibly counter intuitive, the rms value will be slightly larger as the ISRF data points are now compared with a smoothed ISRF instead of an optimized local ISRF that might be influenced by measurement imperfections.

### 3.6 ISRF parameter iteration

An ISSF has typically only 4-5 spectral pixels with sufficient signal-to-noise ratio. Therefore, only fitting with a few parameters is accurate, yielding significant errors in the resulting ISRF. An iterative approach has been developed, starting with a symmetric model without tails. Once the ISRF has been fitted, the skew and tails are known approximately, and can be included as fixed properties while the ISSF is fitted again. The ISRF fit also benefits from a reduction of the number of parameters. Therefore, the refitted block width as a function of row and column is smoothed and used as a fixed property in the final ISRF fit. In the

Atmos. Meas. Tech. Discuss., https://doi.org/10.5194/amt-2017-438
Manuscript under review for journal Atmos. Meas. Tech.
Discussion started: 15 December 2017


Atmospheric Measurement Techniques Discussions

end, the ISSF and ISRF are determined in four passes or 'stages'. The differences between the parameter fitting in ISSF and ISRF fits in the different stages are summarized in Table 1.

The procedure and number of stages have been verified using synthetic ISRF data. To illustrate the ISRF parameter iteration, we present the results of simulations using two realistic ISRFs, one nearly-symmetric and the other skewed. The calculations are performed without noise, and the ISRF is kept constant in each data set. A simulated measurement data set was constructed given the shape of the ISRF and assuming a laser scanning over about 20 spectral pixels in small steps (100 per spectral pixel) similar to the actual calibration measurements. Table 2 lists the intermediate results of the ISRF fit at the end of each stage, while Fig. 2 shows the convergence of the ISRF model towards the true ISRF.

The ISRF parameters of the skewed model are derived with high accuracy (better than 0.5%) after 3 stages. In contrast, the parameter iteration has problems deriving the ISRF tail parameters for the nearly symmetric ISRF, where the tail width is overestimated by more than 20% and the tail fraction is underestimated by 25%. The curve-fitting routine is not the problem, because Fig. 2c shows that the fit residuals are almost zero after stage 3. Apparently, in the case of a symmetric function the algorithm converges to a sub-optimal solution. In this case the algorithm has difficulty separating the nearly symmetric peak from the also symmetric tail function. However, the differences between the true ISRF and the derived ISRF are less than 0.25% and are considered acceptable. The algorithm converges in two stages, see Fig. 2b and 2d. Any further iterations will only marginally improve the results. This is true for noiseless synthetic data, and it should be noted that performing stage 3 does improve the derived ISRF parameters of real measurements. Stage 4 is added because the block width is fixed to its model (derived in the previous stage) in the ISRF fit. This turns out to reduce the variance in the tail parameters significantly.

## 4 Discussion of results

Typical examples of various shapes of the TROPOMI-SWIR ISRF are illustrated in Fig. 3 (irradiance measurements) and Fig. 4 (radiance measurements). Shown are the stage 4 results of the ISRF for five columns: 128, 300, 540, 726 and 935, respectively. A median has been taken over all rows illuminated. From visual inspection of the displayed ISRFs, one can conclude that: $(i)$ the ISRF is sharper and higher at higher column number (longer wavelength); $(ii)$ the ISRF fit resembles the ISRF data very well, e.g. the residuals are very small, except where small artifacts can be identified in the ISRF data; $(iii)$ the fit residuals of the irradiance ISRF are nearly a factor 2 smaller compared with the radiance ISRF.

The Pearson VII distribution has two parameters to control its shape: $m$ and $\gamma$. When both are free parameters, the median value of $m$ in the successful ISRF fits is 1.65 for radiance measurements and 1.25 for irradiance measurements. The difference is likely due to differences in stray light in these measurements. In all subsequent fitting, shape parameter $m$ is fixed to 1.25 to enhance convergence of the curve-fitting routine and inter-comparison between ISRFs derived from irradiance and radiance measurements. It has to be noted that the contribution of the tail to the ISRF is small ($\leq 10\,\%$) and only significant 1-2 pixels away from the peak. It has been verified that fixing the $m$ parameter has negligible effect on the resulting ISRF and the fit residuals expressed in the rms value.

Atmos. Meas. Tech. Discuss., https://doi.org/10.5194/amt-2017-438
Manuscript under review for journal Atmos. Meas. Tech.
Discussion started: 15 December 2017


Atmospheric Measurement Techniques Discussions

Table 3 summarizes the irradiance ISRF characterization. The number of good fits increases with every stage, except for the final stage where, in the ISRF fit, the block width is fixed to the value obtained in the previous stage. The goal of this final stage is, instead, to increase the quality of the tail fitting. This indeed happens as the standard deviation in the tail parameters is reduced by 30–50 %.

The final results of the irradiance ISRF are presented in the appendix of this article, shown are the value of each ISRF parameters from the ISRF fit and after the bivariate polynomial fitting, see Figs. A1–A4. As an example, the skew-normal width is shown in: Fig. 5a its fitted value, Fig. 5c the bivariate polynomial fit result, and in Fig. 5b the difference between the two. The stripe pattern in Fig. 5a is due to scanning imperfections of the laser. They are removed and interpolated in Fig. 5c, but reappear in the difference plot of Fig. 5b. Conclusions for all fitting parameters are:

- Block width $w$ of the ISRF is determined by the projection of the slit onto the detector and therefore decreases as a function of wavelength. As expected, no variation is seen over the spatial dimension of the detector (swath angle).

- Skew-normal width $d$ shows more fine-scale structure than the other parameters. The pattern is probably due to variations in the sensitive area of the detector as the pattern is also seen in sensitivity plots of the detector alone (Hoogeveen et al., 2013). The fine-scale structures are smoothed in the parameter fit. This only has a minor effect on the quality of the ISRF calibration key data, as will be discussed later in this section.

- Skew parameter $s$ shows that the ISRF is positively skewed ($s > 2$) at shorter wavelengths, and negatively skewed at longer wavelengths, but with a gradient along the swath. It appears the algorithm excludes $s$ values between $-0.6$ and $+0.6$ as the difference between these curves is only very small ($< 10^{-3}$). The parameter fit of $s$ will interpolate this gap, introducing an error in the parameter $s$. However, width parameter $d$ has been designed such that no errors are introduced by the ISRF parameter fit.

- Tail parameters $\eta$ and $\gamma$ show little variation over the swath, but their values can vary greatly from one column to the next. The tails have a low signal ($< 0.01$) outside the peak (see Figs. 3 and 4). The low signal hampers the least-square minimization algorithm, leading to significant variation in the tail parameters. The bivariate fitting reduces the variation over swath and wavelengths.

Figure 6a shows the color-coded rms of the ISRF fits. The pixels classified as good, i.e. meeting the requirement for ISRF knowledge, have an rms residual smaller than 0.004, equal to 1% of the maximum value of the ISRF. The bands with bad or moderate fits are attributed to laser artifacts, except for the columns at both ends, which are not scanned by the laser. The little spots of just a few pixels are caused by bad pixels. The quality of the ISRF fits as determined with the parameters from the bivariate parameter-fitting models shown in Fig. 6b. Here the regions with moderate or bad quality fits are extensions of moderate and bad regions in Fig. 6a. There are a few small regions which coincide with the fine-scale structures visible in the skew-normal width, see for example around row 50 at columns 525 and 610. However, regions with good quality ISRF parameter fits are distributed over the entire array, and the values of the ISRF parameters in these regions are consistent with

Atmos. Meas. Tech. Discuss., https://doi.org/10.5194/amt-2017-438
Manuscript under review for journal Atmos. Meas. Tech.
Discussion started: 15 December 2017




the overall trend. This gives us confidence that our SWIR ISRF characterization is successful, and within the requirement on the knowledge of the ISRF.

In general, the laser performed worse during the radiance measurements, yielding radiance ISRF measurements of poorer quality than the irradiance measurements. This can be seen in Fig. 7, which shows in general higher rms values for the ISRF fits for the radiance measurements. Therefore, the radiance ISRF measurements are used for validation of the SWIR ISRF calibration key data obtained using the irradiance ISRF measurements.

For the comparison of the irradiance ISRF with the radiance ISRF, swath angles with the best spectral coverage and quality are selected. From the radiance and irradiance data the rows at ranges 40–72 and 110–140 are selected. Figure 8 shows the median of the ISRF shape parameters as a function of column (before bivariate parameter fitting). In general, the spread in the irradiance data is larger. This is due to the fact that all irradiance data of a column are taken in a single laser scan, while the radiance data of a column is taken from about 100 laser scans, thus averaging out some of the laser irregularities. The skew-normal width and block width show very good agreement at the right side of the detector, including the wiggles which are also visible in Fig. 5a. On the left side of the detector, the block width of the radiance ISRF tends to be smaller than that of the irradiance ISRF. This subtle difference is attributed to the non-optimal scanning of the laser at these wavelengths. The skew parameter tends to be slightly lower for the radiance measurements. However, the impact on the ISRF of this difference is almost negligible. The tail parameters show reasonable resemblance in the two data sets, given the noise in both parameters.

In conclusion, the differences between the measured radiance and irradiance ISRF are too small to conclude that there is a significant difference between the two. More likely, differences are caused by imperfections of the laser-scan behavior or due to subtle differences in residual stray light. This justifies the use of the irradiance measurements to derive the ISRF calibration key data. Moreover, the radiance measurements effectively provide an independent validation of the derived ISRFs.

## 5 In-flight Monitoring of ISRF

As knowledge of the ISRF is critical for the science results of the SWIR band, it has been decided to include means to monitor possible changes in the ISRF between the on-ground calibration campaign and the first measurements in space, and to monitor the ISRF during the 7 years of operational lifetime. For this, five tunable diode lasers in the SWIR wavelength range are included in the on-board calibration unit. Roughly once per month, the ISRF will be monitored using each laser. The laser wavelengths are scanned by tuning the temperature of the laser using a built-in thermo-electric cooler. The scanning range is about 6 spectral pixels so that the ISRF can be monitored for one or two wavelength pixels per laser. The on-board laser illuminates the SWIR spectrometer via a dedicated diffuser. As the diffuser is not moved during the measurements, there will be speckle. Most speckle is removed by taking the median of the data of all illuminated rows.

During the commissioning phase, in-flight measurements with the on-board lasers will be performed with a moving and a fixed diffuser. The ISRF obtained from these measurements can be compared with the ISRF measured on ground using the external laser and the on-board diode lasers to detect any possible changes. The early in-flight measurements also act as a reference for the ISRF monitoring. The monitoring ISRF is of sufficient quality to check for any degradation of the instrument



but cannot be applied in trace-gas retrieval. Should it be necessary, the on-board diode lasers can be used to recalibrate the ISRF for a significant part of the SWIR band.

With an oscillating diffuser, the ISSF and pixel ISRF are determined in four stages, as described in Sect. 3, except that ISRF parameter smoothing (Sect. 3.5) is calculated from the ISRF fits of the few columns scanned per diode laser. The column dependence of the shape parameters is neglected and the row dependence is smoothed by a second order polynomial.

The monitoring ISRF for each of the five lasers is determined with the algorithm presented in Sect. 3 without iterations. It starts with the ISSF fit of stage 4 where a reference ISRF is used based on smoothed parameters of the given row. Then the median ISRF is calculated from all ISRF data of the central one/two fully-scanned columns, neglecting any row dependence.

The ISRF determination using the diode laser with and without moving on-board diffuser has been tried during the ground test and calibration campaigns. The ISRF measured with the diode lasers is in close agreement with the ISRF calibration data, thus proving the usability of the method and validating the calibration data. The monitoring ISRF deviates from the ISRF calibration data as could be expected. However, it is believed the method is sensitive enough to be used on board for long-term monitoring, being able to distinguish between changes in the real instrument ISRF and changes in the speckle pattern.

## 6 Conclusions

A new and accurate method using a scanning OPO has been developed and applied to characterize the TROPOMI-SWIR ISRF. The ISRF characterization has been performed on the basis of stray-light corrected irradiance measurements. The ISRF is modeled by the weighted sum of functions for the peak and the tails. The peak function is a skew-normal distribution convolved with a block distribution, and the tail function is a Pearson type VII distribution. An iterative scheme to derive the SWIR ISRF has been developed, where the ISRF determined in a previous iteration is used to improve the ISSF model in the current iteration. The required accuracy of the ISRF is obtained within 4 iterations. Each of the five ISRF shape parameters has been smoothed by fitting a bivariate Chebyshev expansion to derive the ISRF calibration key data for all SWIR wavelengths and swath angles.

The ISRF measured through the irradiance port using the solar diffuser has been compared with the equivalent ISRF measured via the radiance port. The differences between the ISRFs derived from both data sets are very small, and largely due to differences in stray-light treatment and laser scan imperfections. The derived ISRF meets the requirement on ISRF knowledge and should thus be sufficient for methane retrievals.

The on-board calibration unit contains five diode lasers in the SWIR wavelength range. These diode lasers will be employed to verify the ISRF calibration key data after launch. During operations, the lasers will be used to monitor the long-term stability of the optical properties of the SWIR module.

## 7 Data availability

The underlying data of the figures presented in this publication can be found at ftp://ftp.sron.nl/open-access-data/richardh.



*Competing interests.* The authors declare that they have no conflict of interest.

*Acknowledgements.* The authors would like to thank the teams of Airbus Defence and Space Netherlands and KNMI for organizing the calibration campaign and in particular the operators for the tireless data acquisition.

TROPOMI is a collaboration between Airbus Defence and Space Netherlands, KNMI, SRON and TNO, on behalf of NSO and ESA. Airbus Defence and Space Netherlands is the main contractor for the design, building and testing of the instrument. KNMI and SRON are the principal investigator institutes for the instrument. TROPOMI is funded by the following ministries of the Dutch government: the Ministry of Economic Affairs, the Ministry of Education, Culture and Science, and the Ministry of Infrastructure and the Environment.



## References

Beers, T. C., Flynn, K., and Gebhardt, K.: Measures of Location and Scale for Velocities in Clusters of Galaxies—A Robust Approach, The Astronomical Journal, 100, 32–46, doi:10.1086/115487, 1990.

Buscaglione, F.: GMES Sentinel-5 Precursor — S5p System Requirement Document (SRD), S5p-RS-ESA-SY-0002, ESA, issue 4.1, 2011.

Hoogeveen, R. W. M., Voors, R., Robbins, M. S., Tol, P. J. J., and Ivanov, T. I.: Characterization results of the TROPOMI Short Wave InfraRed detector, Proceedings of SPIE, 8889, 888–913, doi:10.1117/12.2028759, 2013.

Hu, H., Hasekamp, O., Butz, A., Galli, A., Landgraf, J., aan de Brugh, J., Borsdorff, T., Scheepmaker, R., and Aben, I.: The operational methane retrieval algorithm for TROPOMI, AMT, 9, 5423–5440, 2016.

Kleipool, Q., Babić, L., Bartstra, R., Braak, R., Dierssen, W., Dewitte, P.-J., Kenter, P., Leloux, Jonatan, L. E., Ludewig, A., Meijering, P., van der Plas, E., Rozemeijer, N., Schepers, D., Schiavini, D., Smeets, J., Vacanti, G., and Vonk, F.: Pre-launch calibration status of the TROPOMI payload on-board the Sentinel 5 precursor satellite, submitted to Atmos. Meas. Tech., 2017.

Patefield, M. and Tandy, D.: Fast and Accurate Calculation of Owen's T Function, Journal of Statistical Software, 5, 1–25, http://people.sc.fsu.edu/~jburkardt/f_src/owens/owens.html, 2000.

Tol, P. J. J., van Kempen, T. A., van Hees, R. M., Krijger, M., Cadot, S., Aben, I., Persijn, S. T., and Hoogeveen, R. W. M.: Characterization and correction of stray light in TROPOMI-SWIR, submitted to Atmos. Meas. Tech., 2017.

van Amerongen, A., Krol, H., Grèzes-Besset, C., Coppens, T., Bhatti, I., Lobb, D., Hardenbol, B., and Hoogeveen, R. W. M.: State of the art in silicon immersed gratings for space, Proceedings of the International Conference on Space Optics, 2012.

Veefkind, J. P., Aben, I., McMullan, K., Förster, H., De Vries, J., Otter, G., Claas, J., Eskes, H. J., De Haan, J. F., Kleipool, Q., van Weele, M., Hasekamp, O., Hoogeveen, R. W. M., Landgraf, J., Snel, R., Tol, P., Ingmann, P., Voors, R., Kruizinga, B., Vink, R., Visser, H., and Levelt, P. F.: TROPOMI on the ESA Sentinel-5 Precursor: A GMES mission for global observations of the atmospheric composition for climate, air quality and ozone layer applications, Remote Sensing of Environment, 120, 70–83, doi:10.1016/j.rse.2011.09.027, 2012.

Atmos. Meas. Tech. Discuss., https://doi.org/10.5194/amt-2017-438
Manuscript under review for journal Atmos. Meas. Tech.
Discussion started: 15 December 2017


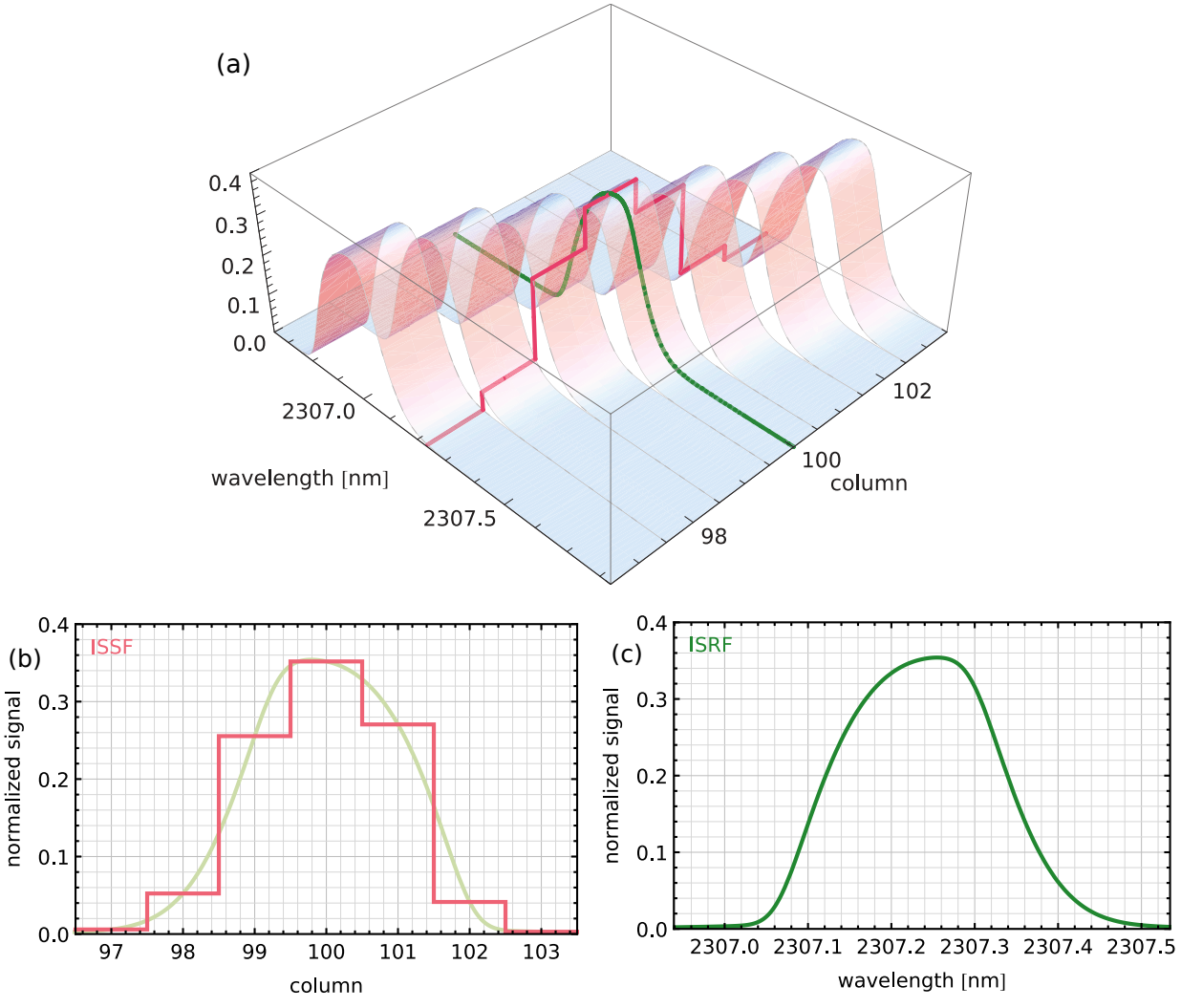


**Figure 1.** Normalized signal as a function of source wavelength and pixel on an arbitrary row, with two cross sections: the ISSF at 2307.24 nm (red) and the ISRF of the pixel in column 100 (green). In the plot of the ISSF, a mirrored version of the ISRF is shown in light green. The skew of the ISRF has been exaggerated to show the mirroring.

Atmos. Meas. Tech. Discuss., https://doi.org/10.5194/amt-2017-438
Manuscript under review for journal Atmos. Meas. Tech.
Discussion started: 15 December 2017


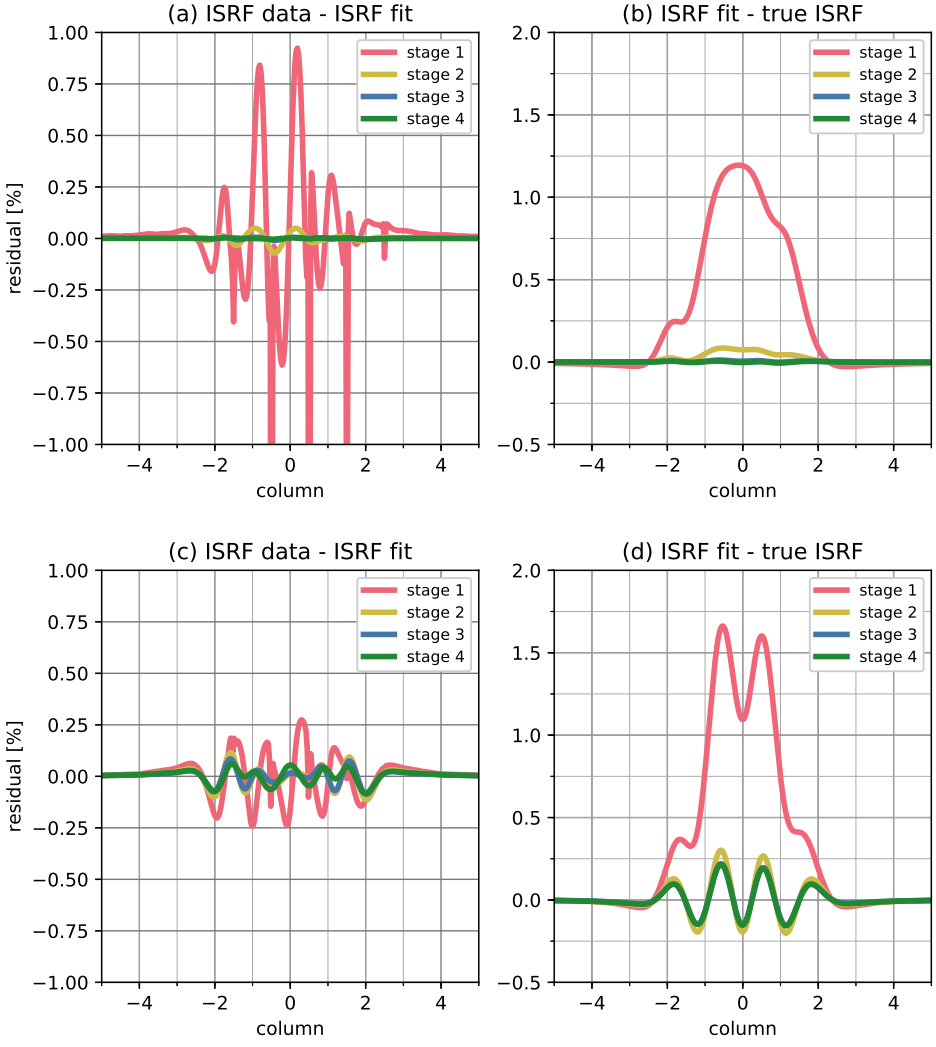


**Figure 2.** Convergence of the ISRF model towards a synthetic ISRF using the ISRF parameter iteration. The results for the 'skewed' synthetic ISRF are shown in panels (a) and (b), where panel (a) shows the relative difference between the ISRF data and the ISRF fit, and panel (b) shows the relative difference between the ISRF fit and the 'true' ISRF. Panel (c) and (d) show the results for the 'symmetric' synthetic ISRF.

Atmos. Meas. Tech. Discuss., https://doi.org/10.5194/amt-2017-438
Manuscript under review for journal Atmos. Meas. Tech.
Discussion started: 15 December 2017


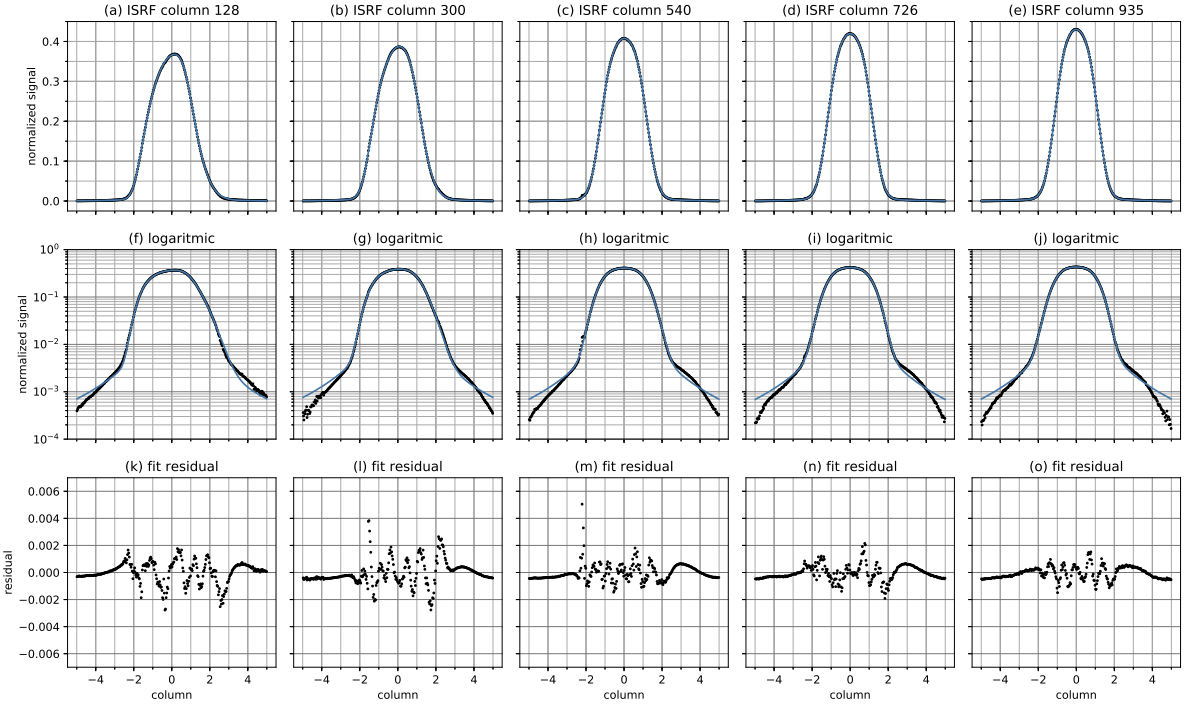


**Figure 3.** Examples of the median irradiance ISRF data with fits. The ISRF fit parameter values of the columns 128, 300, 540, 726 and 935 are respectively: (skew-normal width) 0.575, 0.509, 0.444, 0.432 and 0.425; (skew) 2.880, 2.062, 0.825, 0.334 and -0.689; (block width) 2.669, 2.594, 2.461, 2.388 and 2.301; (tail fraction) 0.081, 0.108, 0.101, 0.103 and 0.097; (tail shape) 1.25; (tail width) 1.158, 0.988, 0.972, 0.952 and 1.010. The plots show the data and fits on a linear (top) and logarithmic (middle) scale. The residuals are shown in the bottom plots.

Atmos. Meas. Tech. Discuss., https://doi.org/10.5194/amt-2017-438
Manuscript under review for journal Atmos. Meas. Tech.
Discussion started: 15 December 2017


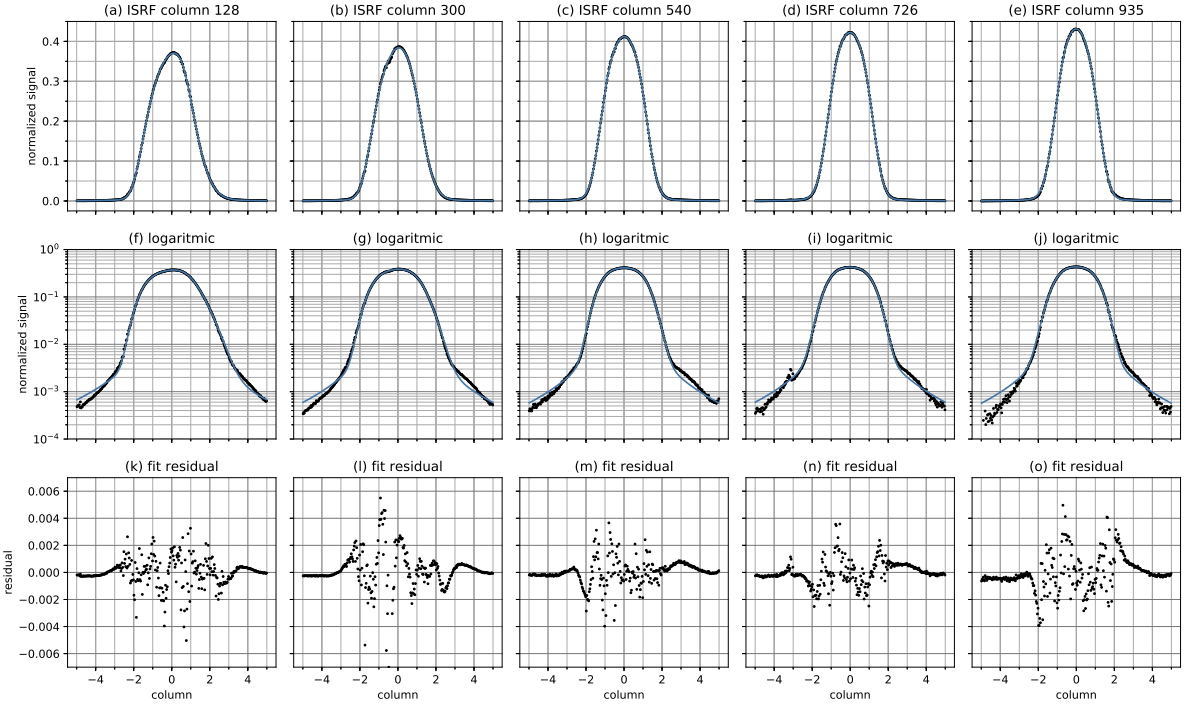


**Figure 4.** As in Fig. 3, for radiance measurements. The ISRF fit parameter values of the columns 128, 300, 540, 726 and 935 are respectively: (skew-normal width) 0.620, 0.527, 0.444, 0.445 and 0.451; (skew) 2.569, 1.650, 0.786, -0.701 and -0.879; (block width) 2.641, 2.607, 2.452, 2.363 and 2.307; (tail fraction) 0.079, 0.108, 0.110, 0.100 and 0.106; (tail shape) 1.65; (tail width) 1.625, 1.238, 1.142, 1.235 and 1.196.

Atmos. Meas. Tech. Discuss., https://doi.org/10.5194/amt-2017-438
Manuscript under review for journal Atmos. Meas. Tech.
Discussion started: 15 December 2017


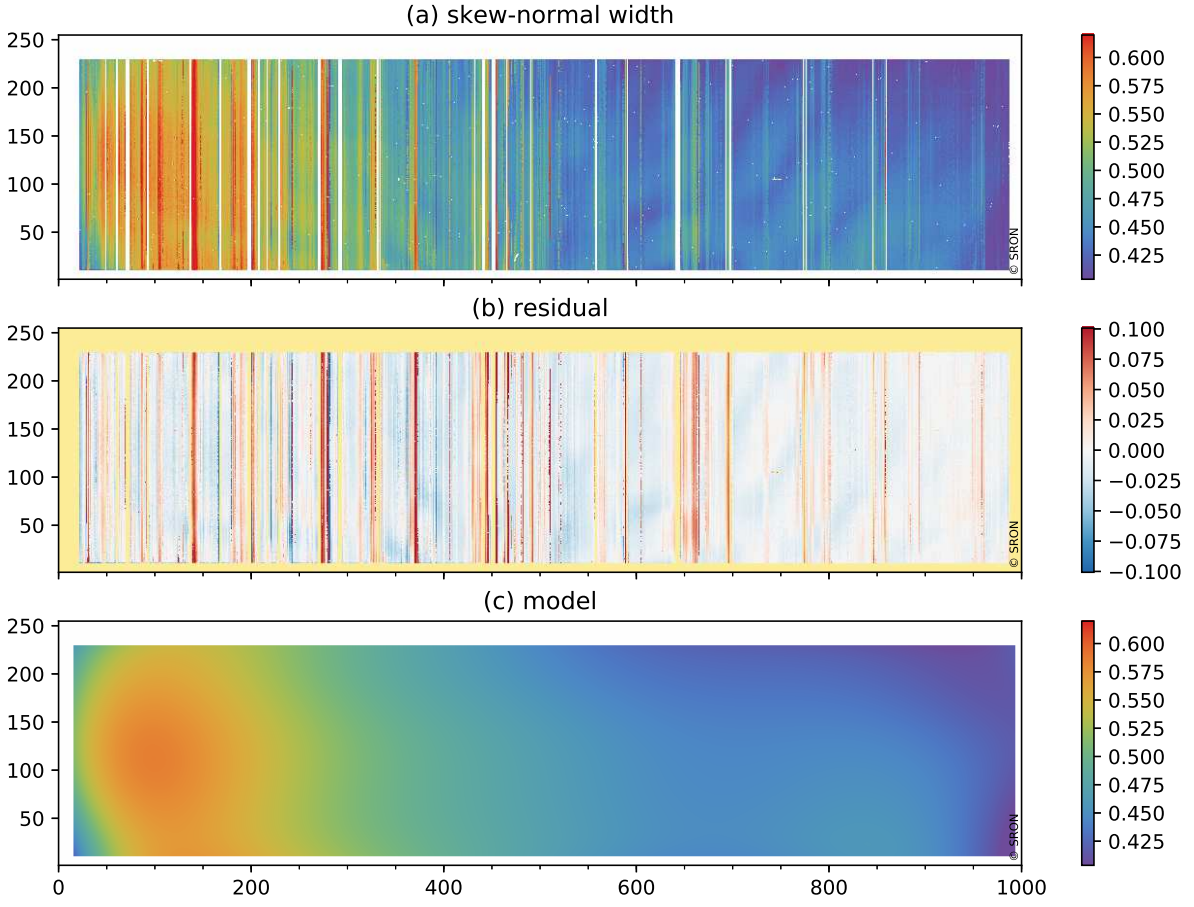


**Figure 5.** Irradiance ISRF fit results for the peak function (final): skew-normal width $d$. Presented are (a) ISRF fit, (c) ISRF parameter fit, and (b) the difference between the two. In the white area, the ISRF fit failed (vertical stripes), the light is blocked by the entrance slit of the spectrometer (top and bottom) or a shield at the detector (left and right). The white spots are bad pixels.

Atmos. Meas. Tech. Discuss., https://doi.org/10.5194/amt-2017-438
Manuscript under review for journal Atmos. Meas. Tech.
Discussion started: 15 December 2017


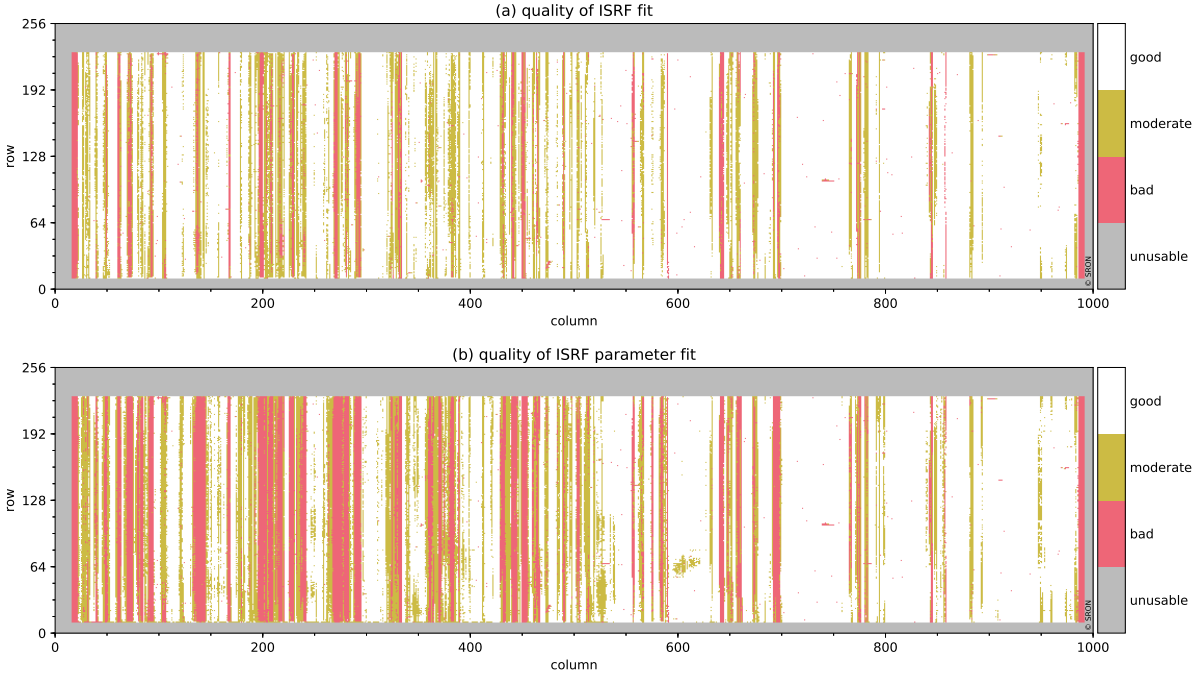


**Figure 6.** Irradiance ISRF fit results: (a) quality of ISRF fit and (b) quality of ISRF parameter fit, based on the rms value. The threshold between good and moderate is 0.004 and between moderate and bad 0.0065. In the gray area, the light is blocked by the entrance slit of the spectrometer (top and bottom) or by the shield at the detector (left and right).

Atmos. Meas. Tech. Discuss., https://doi.org/10.5194/amt-2017-438
Manuscript under review for journal Atmos. Meas. Tech.
Discussion started: 15 December 2017


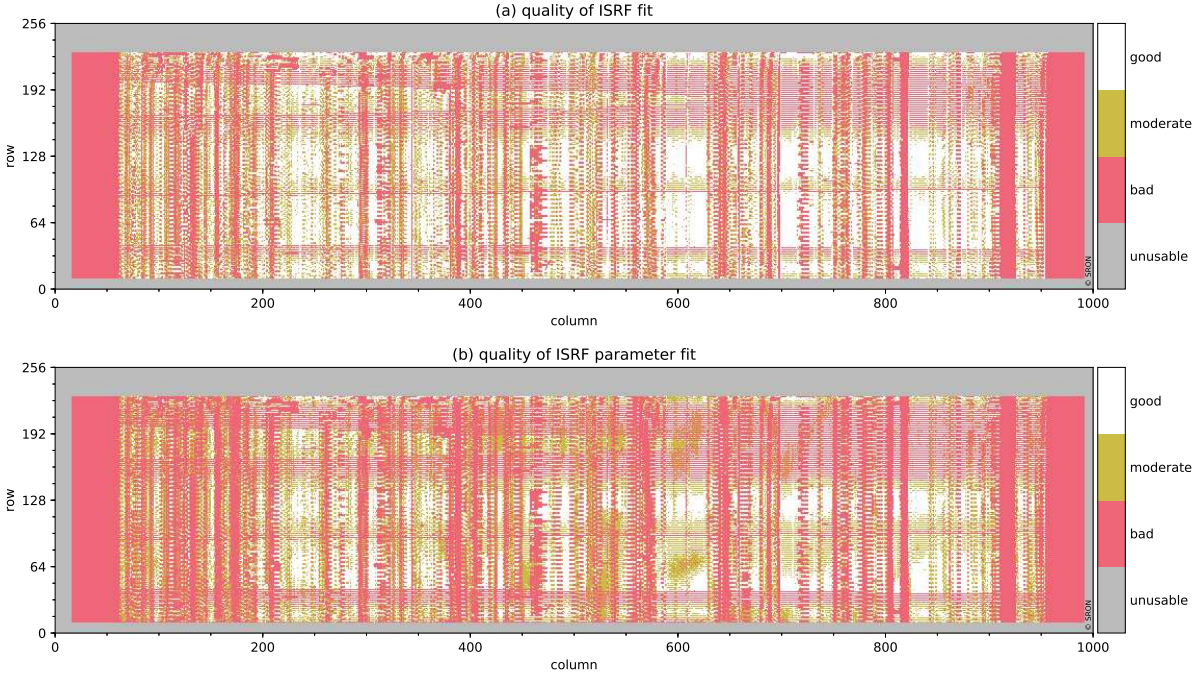


**Figure 7.** Same as Fig. 6, except for the radiance ISRF.

Atmos. Meas. Tech. Discuss., https://doi.org/10.5194/amt-2017-438
Manuscript under review for journal Atmos. Meas. Tech.
Discussion started: 15 December 2017


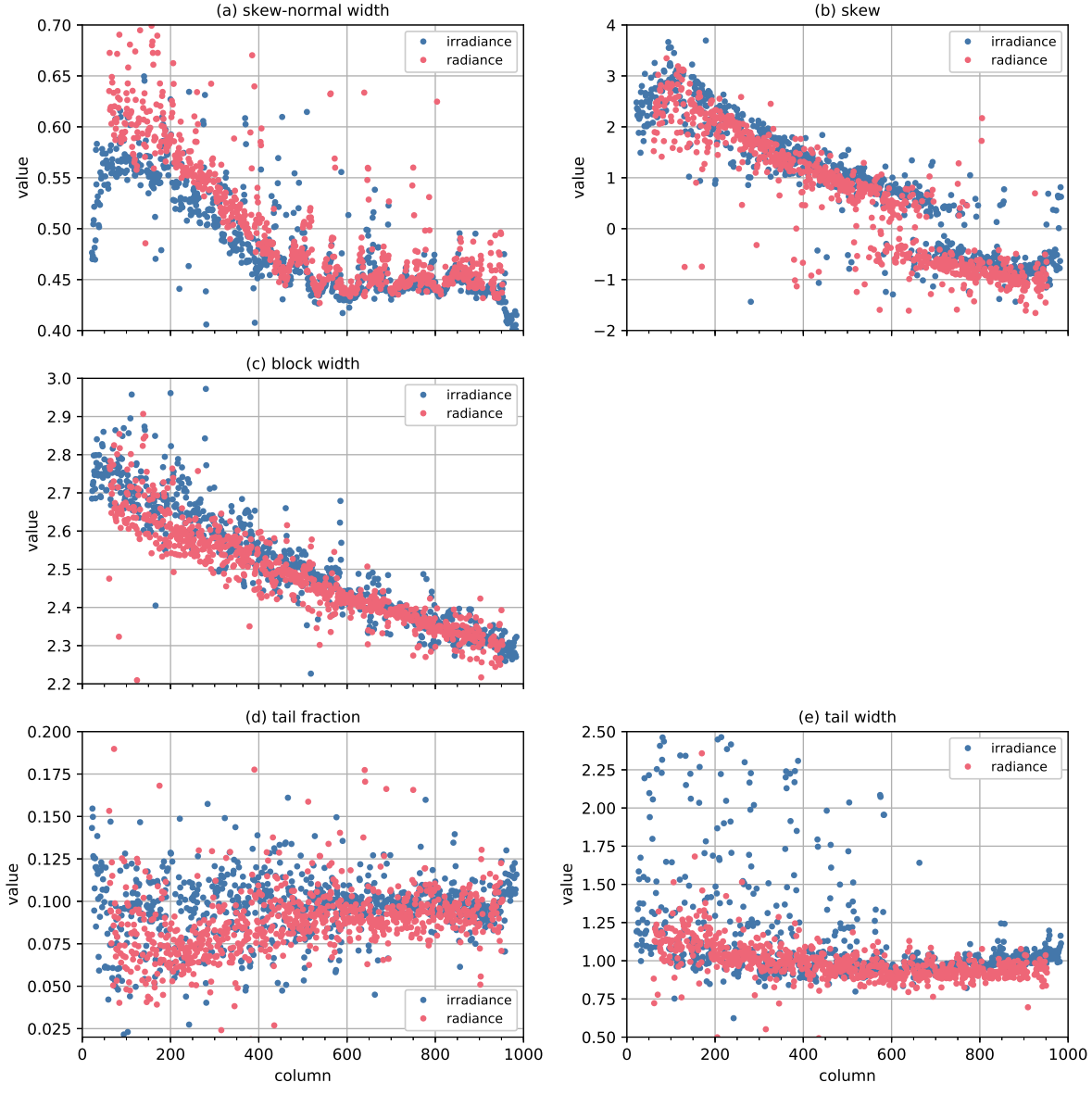


**Figure 8.** Comparison of the five ISRF parameters derived from irradiance and radiance measurements: as a function of column.

Atmos. Meas. Tech. Discuss., https://doi.org/10.5194/amt-2017-438
Manuscript under review for journal Atmos. Meas. Tech.
Discussion started: 15 December 2017


Atmospheric Measurement Techniques Discussions

**Table 1.** Treatment of parameters in each stage and for each type of data set: either hold constant (entry is a number), interpolate the previous ISRF results (entry 'model') or include in the fit (entry 'fit'). In the case of $s$ for ISSF fits, the interpolated value is given the opposite sign, to take into account that an ISSF is basically the mirrored version of an ISRF.

| stage | data | $A$ | $c_0$ | $d$ | $s$ | $w$ | $\gamma$ | $m$ | $\eta$ |
|---|---|---|---|---|---|---|---|---|---|
| 1 | ISSF | fit | fit | fit | 0 | fit | 1 | 1.25 | 0 |
| | ISRF | fit | fit | fit | fit | fit | fit | 1.25 | fit |
| 2 | ISSF | fit | fit | fit | model | fit | model | 1.25 | model |
| | ISRF | fit | fit | fit | fit | fit | fit | 1.25 | fit |
| 3 | ISSF | fit | fit | fit | model | fit | model | 1.25 | model |
| | ISRF | fit | fit | fit | fit | fit | fit | 1.25 | fit |
| 4 | ISSF | fit | fit | fit | model | model | model | 1.25 | model |
| | ISRF | fit | fit | fit | fit | model | fit | 1.25 | fit |

**Table 2.** Listing the intermediate parameters of the derived ISRF from two synthetic ISRF data sets: 'skew' and 'symmetric'. The ISRF parameter iteration is performed, as defined in Table 1, except that no ISRF parameter smoothing was necessary. The shape parameters for the true ISRF are listed in italic.

| | stage | $d$ | $s$ | $w$ | $\gamma$ | $m$ | $\eta$ |
|---|---|---|---|---|---|---|---|
| skew | 1 | 0.514 | 1.975 | 2.585 | 0.101 | 1.25 | 0.997 |
| | 2 | 0.511 | 2.049 | 2.589 | 0.106 | 1.25 | 0.995 |
| | 3 | 0.510 | 2.058 | 2.592 | 0.107 | 1.25 | 0.992 |
| | 4 | 0.510 | 2.059 | 2.592 | 0.107 | 1.25 | 0.992 |
| | true | *0.509* | *2.062* | *2.594* | *0.108* | *1.25* | *0.988* |
| symmetric | 1 | 0.457 | 0.295 | 2.321 | 0.044 | 1.25 | 1.956 |
| | 2 | 0.449 | 0.318 | 2.337 | 0.069 | 1.25 | 1.276 |
| | 3 | 0.445 | 0.324 | 2.350 | 0.079 | 1.25 | 1.142 |
| | 4 | 0.445 | 0.325 | 2.350 | 0.079 | 1.25 | 1.141 |
| | true | *0.432* | *0.334* | *2.388* | *0.103* | *1.25* | *0.952* |

Atmos. Meas. Tech. Discuss., https://doi.org/10.5194/amt-2017-438
Manuscript under review for journal Atmos. Meas. Tech.
Discussion started: 15 December 2017


Atmospheric Measurement Techniques Discussions

**Table 3.** Summary of the irradiance ISRF characterization. Listed are for the 4 stages: the quality of the ISRF fit, the average and uncertainty over the complete array of the rms, $d$, $s$, $w$, $\eta$ and $\gamma$, and the residuals between these parameter values and the parameter fits. To avoid the effect of outliers, the biweight estimate of location and scale are used for the average and uncertainty, respectively (Beers et al., 1990).

| fit parameter | | stage 1 | stage 2 | stage 3 | stage 4 |
|---|---|---|---|---|---|
| quality | good | 142409 | 164012 | 164646 | 160161 |
| | moderate | 53253 | 35639 | 35118 | 36560 |
| | bad | 13296 | 9907 | 9604 | 12946 |
| | failed | 2617 | 2015 | 2206 | 1907 |
| rms $[10^{-3}]$ | median | $3.15 \pm 1.68$ | $2.44 \pm 1.41$ | $2.41 \pm 1.40$ | $2.53 \pm 1.49$ |
| skew-normal width $d$ | median | $0.479 \pm 0.058$ | $0.473 \pm 0.060$ | $0.470 \pm 0.060$ | $0.471 \pm 0.058$ |
| | residual | $-0.003 \pm 0.028$ | $-0.004 \pm 0.025$ | $-0.004 \pm 0.025$ | $-0.005 \pm 0.020$ |
| skew $s$ | median | $0.940 \pm 1.164$ | $1.005 \pm 1.204$ | $1.018 \pm 1.207$ | $1.019 \pm 1.181$ |
| | residual | $0.018 \pm 0.490$ | $0.017 \pm 0.442$ | $0.012 \pm 0.439$ | $0.010 \pm 0.417$ |
| block width $w$ | median | $2.484 \pm 0.176$ | $2.494 \pm 0.168$ | $2.501 \pm 0.166$ | — |
| | residual | $-0.003 \pm 0.052$ | $-0.004 \pm 0.049$ | $-0.003 \pm 0.049$ | — |
| tail fraction $\eta$ | median | $0.075 \pm 0.029$ | $0.087 \pm 0.029$ | $0.092 \pm 0.029$ | $0.097 \pm 0.019$ |
| | residual | $-0.001 \pm 0.029$ | $-0.001 \pm 0.029$ | $-0.001 \pm 0.029$ | $-0.001 \pm 0.019$ |
| tail width $\gamma$ | median | $1.240 \pm 0.562$ | $1.048 \pm 0.321$ | $1.004 \pm 0.255$ | $0.988 \pm 0.131$ |
| | residual | $0.231 \pm 0.558$ | $0.066 \pm 0.298$ | $0.040 \pm 0.218$ | $0.009 \pm 0.101$ |

Atmos. Meas. Tech. Discuss., https://doi.org/10.5194/amt-2017-438
Manuscript under review for journal Atmos. Meas. Tech.
Discussion started: 15 December 2017


Atmospheric Measurement Techniques Discussions

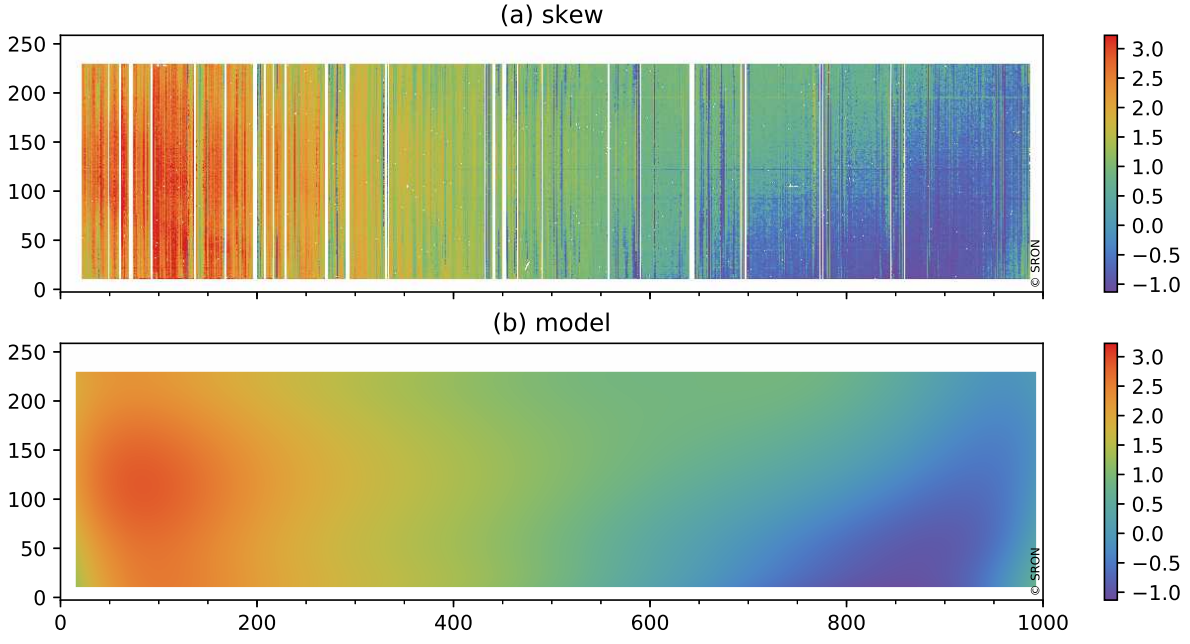


**Figure A1.** Irradiance ISRF fit results for the peak function (final): skew $s$. Presented are (a) ISRF fit and (b) ISRF parameter fit, see also Fig. 5.

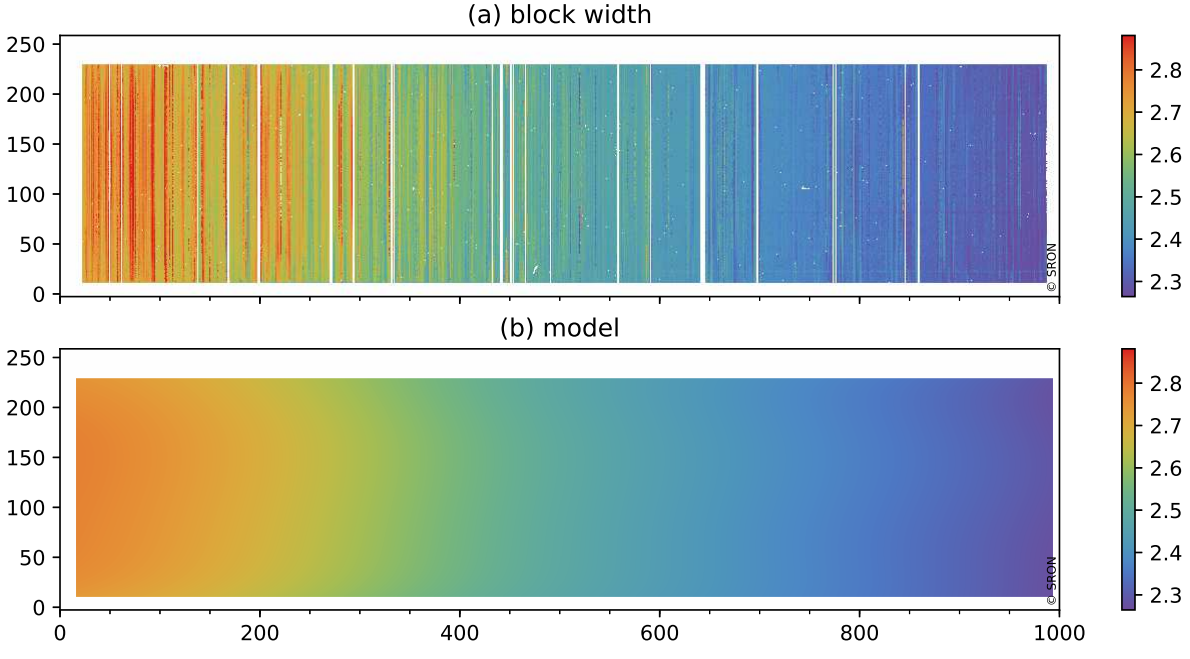


**Figure A2.** Same as Fig. A1, except for block width $w$.

Atmos. Meas. Tech. Discuss., https://doi.org/10.5194/amt-2017-438
Manuscript under review for journal Atmos. Meas. Tech.
Discussion started: 15 December 2017


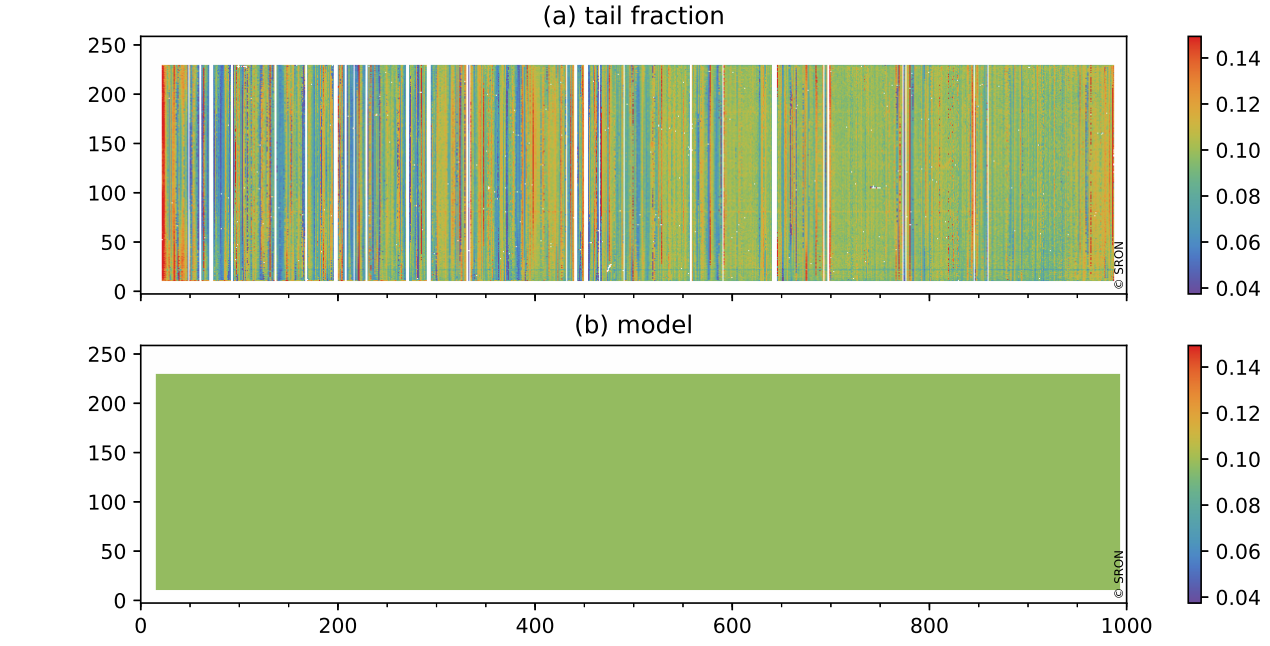


**Figure A3.** Same as Fig. A1, except for tail fraction $\eta$.

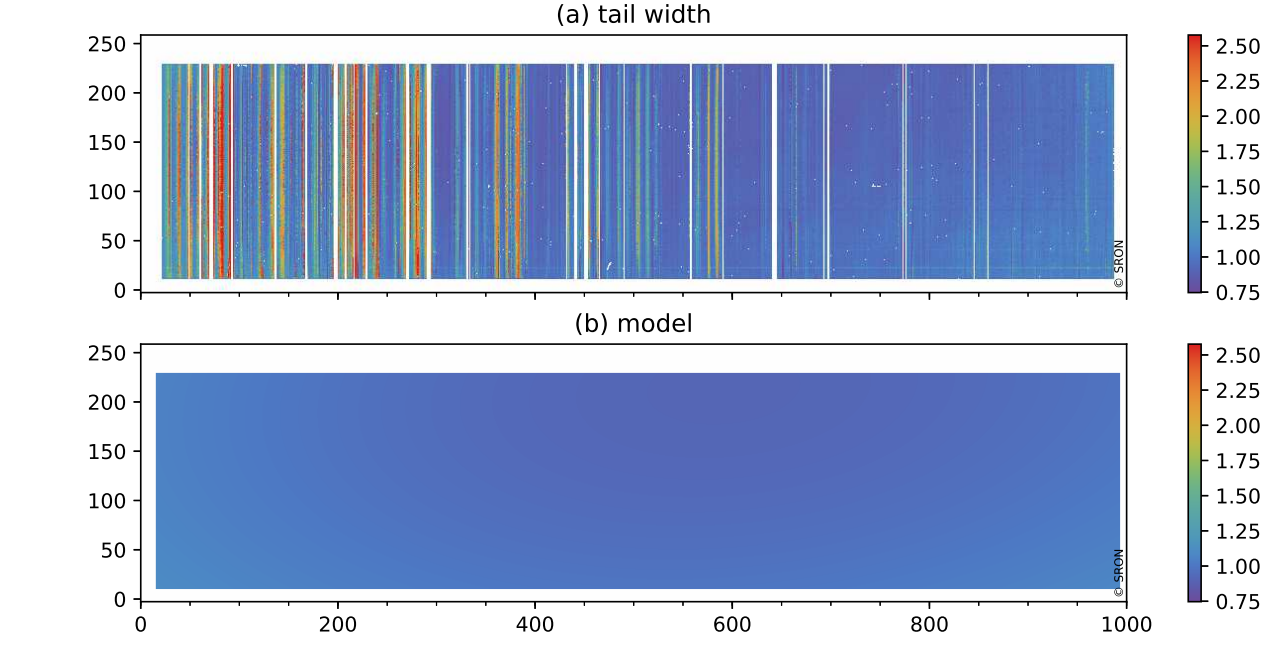


**Figure A4.** Same as Fig. A1, except for tail width $\gamma$.